Terahertz Emission From an Exchange-Coupled Synthetic Antiferromagnet

Qi Zhang[1,2] Yumeng Yang,[2,3] Ziyan Luo,[2] Yanjun Xu,[2] Rongxiang Nie[4] Xinhai Zhang,[1,*] and
Yihong Wu[2,†]

[1]*Department of Electrical and Electronic Engineering, Southern University of Science and Technology,
Xueyuan Rd 1088, Shenzhen 518055, China*

[2]*Department of Electrical and Computer Engineering, National University of Singapore, 4 Engineering Drive 3,
Singapore 117583, Singapore*

[3]*School of Information Science and Technology, ShanghaiTech University, 393 Middle Huaxia Road,
Shanghai 201210, China*

[4]*NUS (Suzhou) Research Institute, National University of Singapore, No. 377 Linquan Street, Suzhou 215123,
China*

We report on terahertz emission from Fe-Mn-Pt/Ru/Fe-Mn-Pt and Pt/Co-Fe-B/Ru/Co-Fe-B/Pt synthetic antiferromagnet (SAF) structures upon irradiation by a femtosecond laser; the former is via the anomalous Hall effect, whereas the latter is through the inverse spin Hall effect. The antiparallel alignment of the two ferromagnetic layers leads to a terahertz emission peak amplitude that is almost double that of a corresponding single-layer or bilayer emitter with the same equivalent thickness. In addition, we demonstrate by both simulation and experiment that terahertz emission provides a powerful tool to probe the magnetization reversal processes of individual ferromagnetic layers in a SAF structure, as the terahertz signal is proportional to the vector difference ($\mathbf{M}_1 - \mathbf{M}_2$) of the magnetizations of the two ferromagnetic layers.

I. INTRODUCTION

Recently, spin-to-charge conversion in femtosecond-laser-excited magnetic heterostructures has attracted attention as a promising mechanism for producing high-efficiency and wide-bandwidth terahertz emission with a magnetically controllable polarization state [1]. The key to this terahertz emission is the generation of a spin-polarized superdiffusive charge current from a ferromagnetic layer by femtosecond laser excitation and subsequent conversion of the spin current to a transverse charge current, thereby generating terahertz emission. The two widely studied spin-to-charge conversion mechanisms are the inverse spin Hall effect (ISHE) [1–12] and the inverse Rashba-Edelstein effect (IREE) [13–15]. The former involves a ferromagnet (FM)/nonmagnet (NM) heterostructure where, when a femtosecond laser irradiates the heterostructure, nonequilibrium electrons are excited to states above the Fermi level, generating a spin-polarized superdiffusive current flowing from the FM to the NM layer [16,17]. The superdiffusive transient current is subsequently converted to a transverse charge current in the NM layer with a large spin-orbit coupling and thus gives rise to terahertz emission [1,2]. On the other hand, the terahertz emitter based on the IREE typically consists of a FM with an adjacent Rashba interface, e.g., FM/Ag/Bi [18]; in this case, the superdiffusive spin-polarized current launched from the FM layer is converted to a transverse charge current at the Ag/Bi interface via the IREE [13–15], which, in the same way as the ISHE, generates terahertz emission. Recently, we have demonstrated an alternative way to generate terahertz emission from a single-layer FM that involves the generation of a backflow nonthermal charge current from the ferromagnet/dielectric interface by femtosecond laser excitation and subsequent conversion of the charge current to a transverse transient charge current via the anomalous Hall effect (AHE), thereby generating terahertz radiation [19]. The terahertz emission can be either enhanced or suppressed, or the polarity can even be reversed, by introducing a magnetization gradient in the thickness direction of the ferromagnet. Unlike spintronic terahertz emitters based on the ISHE or IREE, an AHE-based emitter does not require an additional nonmagnetic layer or Rashba interface.

In this paper, we investigate terahertz emission from exchange-coupled synthetic antiferromagnets (SAFs). Two types of SAF structure are studied, namely,

---

*zhangxh@sustc.edu.cn
†elewuyh@nus.edu.sg

Fe-Mn-Pt/Ru/Fe-Mn-Pt and Pt/Co-Fe-B/Ru/Co-Fe-B/ Pt. The former uses the AHE and the latter uses the ISHE to generate the terahertz emission. The atomic compositions of the Fe-Mn-Pt and Co-Fe-B alloys are $(Fe_{0.8}Mn_{0.2})_{0.67}Pt_{0.33}$ and $Co_{0.2}Fe_{0.6}B_{0.2}$, respectively, unless otherwise specified. The motivations are twofold. First, an enhancement of terahertz emission is anticipated in both cases when the magnetizations of the two FM layers are aligned antiparallel; this is because in both structures the longitudinal superdiffusive currents would flow in opposite directions in the two FM layers. Second, since the polarization of the terahertz emission is determined by the directions of both the superdiffusive current and the magnetization, the terahertz emission may provide a powerful tool to probe the magnetization reversal process in SAFs, which are an important constituent of all types of spintronic devices. Experimentally, we indeed find that there is a significant enhancement of terahertz emission for these SAF structures compared with single-layer Fe-Mn-Pt or Co-Fe-B/Pt bilayer emitters with the same equivalent thickness (it is nearly doubled). Through both simulation and experiments, we show that the polarization of the terahertz waves provides additional insight into the magnetization reversal process of the SAF that cannot be obtained from standard magnetometry measurements. This is because the superdiffusive currents function effectively as two independent probes of the two FM layers, instead of the single probe provided by the pump laser. The rest of the paper is organized as follows. Section II deals with macrospin modeling of terahertz emission from SAF structures, in which we show how the terahertz polarization is dependent on the magnetization directions of the individual FM layers. The experimental details are given in Sec. III. In Sec. IV, we present experimental results on both types of SAF structure, including their magnetic properties and the characteristics of their terahertz emission, based on which conclusions are drawn.

II. MACROSPIN MODELING OF TERAHERTZ EMISSION FROM SAF STRUCTURES

Before we discuss the experimental details, we first describe the simulation of the terahertz emission from a SAF using a macrospin model, and compare the results with the hysteresis curve obtained from magnetometry measurements. Figures 1(a) and 1(b) show the structures of the two types of SAF. Also shown are the coordinate systems [Fig. 1(c)] that are used in the discussion throughout this paper. Here, the films are in the xy plane, and both the excitation laser beam and the terahertz wave propagate in the z direction. Although both samples have a SAF structure, the key difference is that the first structure (which we refer to hereafter as the Fe-Mn-Pt SAF) does not have any heavy-metal (HM) layers on the two
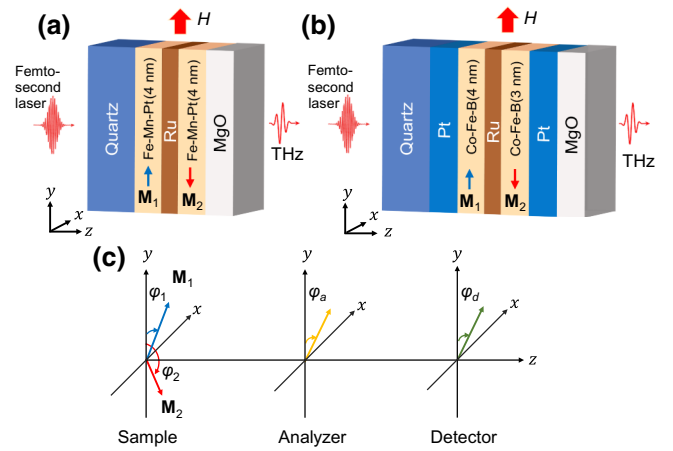

FIG. 1. Schematic illustration of the (a) Fe-Mn-Pt SAF and (b) Co-Fe-B SAF structures used in this study. (c) Schematic illustration of the coordinate systems used for terahertz detection.

sides, whereas the second structure consists of a SAF sandwiched between two Pt layers (which we refer to hereafter as the Co-Fe-B SAF). Upon femtosecond laser irradiation, spin-polarized superdiffusive currents are generated in both the Fe-Mn-Pt and the Co-Fe-B layers. In the case of the Fe-Mn-Pt SAF, the superdiffusive currents are reflected back from both the left (with the quartz substrate) and the right (with the MgO capping layer) interfaces, and are subsequently converted to a transverse charge currents via the AHE to generate terahertz emission. Since the backflow currents from the two interfaces have opposite directions, the net transverse charge-current density can be written as $\mathbf{j}_c \propto (\mathbf{M}_1 - \mathbf{M}_2) \times \hat{\mathbf{z}}$, where $\hat{\mathbf{z}}$ is a unit vector along the z axis. On the other hand, for the Co-Fe-B SAF, the superdiffusive currents generated in the two FM layers enter their respective adjacent Pt layers, where they are converted to transverse charge currents via the ISHE, which eventually results in the emission of a terahertz wave. Similarly to the case of the Fe-Mn-Pt SAF, the net transverse charge-current density can be written as $\mathbf{j}_c \propto -(\mathbf{M}_1 - \mathbf{M}_2) \times \hat{\mathbf{z}}$. The difference, if any, is just in the sign, which depends on the relative magnitudes of the superdiffusive currents in the two layers and on the transparencies of the interfaces, which are not always the same. These simple facts show that terahertz generation in the two SAF structures can be modeled using a macrospin model on an equal footing, despite the fact that they are based on different mechanisms. The amplitude of the terahertz wave detected by the detector depends on the relative orientation of the magnetization of the FM layers, the polarization axis of the analyzer, and the crystal direction of the ZnTe detector. Without losing generality, we assume that the polarization axis of the wire-grid analyzer and the detection axis of the ZnTe detector are at angles of φ_a and φ_d [20], respectively, away from the y axis [Fig. 1(c)]. Similarly, the directions of

M_1 and M_2 are defined by φ_1 and φ_2, respectively (assuming both are in the plane). We use the convention that φ_1 and φ_2 are positive when they rotate away from the positive y to the negative x axis (counterclockwise rotation) and negative when they rotate in the opposite direction. By using this sign convention and the coordinate system in Fig. 1(c), the detected electric field of the terahertz emission may be written as

$$\mathbf{E}_{\text{THz}} \propto \pm[(M_1 \cos \varphi_1 - M_2 \cos \varphi_2) \sin \varphi_a \sin \varphi_d, (M_2 \sin \varphi_2 - M_1 \sin \varphi_1) \cos \varphi_a \cos \varphi_d, 0]. \tag{1}$$

Here we assume that the spin-polarized superdiffusive current is proportional to the magnetization. Although there is no rigorous basis for this assumption, it does not affect the discussion, because we are interested only in the direction of this current rather than its absolute value. The sign before the square brackets depends on the direction of the spin-polarized current that contributes to terahertz emission in the two SAFs, i.e., positive for the Fe-Mn-Pt SAF and negative for the Co-Fe-B SAF. If we let $\varphi_a = \varphi_d = \pi/2$, then $\mathbf{E}_{\text{THz}}$ has only an x component, which is given by $E_x \propto \pm(M_1 \cos \varphi_1 - M_2 \cos \varphi_2) = \pm(M_{1y} - M_{2y}) = \pm\Delta M_y$. Similarly, when $\varphi_a = \varphi_d = 0$, there is only a y component, given by $E_y \propto \pm(M_2 \sin \varphi_2 - M_1 \sin \varphi_1) = \pm(M_{2x} - M_{1x}) = \mp\Delta M_x$. It is apparent that the terahertz emission will be maximum when the two layers are antiparallel to each other. The amplitude of the terahertz wave will be simply the sum of the contributions from the two layers, which means that theoretically it could be doubled compared with a single-layer emitter of the same equivalent thickness if the effect of the Ru is small. The latter is a reasonable assumption because (i) the superdiffusive currents from the two sides of the Ru are presumably cancelled out by each other and (ii) Ru has a relatively small spin Hall angle compared with other heavy metals used in spintronic terahertz emitters [2,12,21,22]. Moreover, the superdiffusive current that crosses over the Ru layer and enters the other side of the Fe-Mn-Pt creates a desirable effect because it increases the difference in backflow current between the FM/oxide and FM/Ru interfaces. The simple relationship derived above may serve as a powerful tool to study the magnetization reversal process of a SAF when it is subjected to a sweeping magnetic field. By examining the signs of E_x and E_y, one should be able to find out in which direction and how the magnetizations of the two FM layers respond to the sweeping external field. The information obtained should be very useful for gaining insight into the exchange coupling in the SAF, which is important for device applications. In contrast, standard magnetometry measurements can provide information about only the overall projection of the magnetizations of the two layers, i.e., $M_y = M_1 \cos \varphi_1 + M_2 \cos \varphi_2$; it is difficult to probe the magnetization directions of the individual layers, which are crucial for understanding the magnetization reversal process.

To obtain a more quantitative understanding of the difference between the information obtained from terahertz and magnetometry measurements, we first conduct macrospin modeling of the SAF structures. For a SAF consisting of two magnetic layers with uniaxial magnetic anisotropy, in the coordinate system of Fig. 1(c), the energy per unit area as a function of an in-plane magnetic field (H) is given by

$$E = K_{u1}d_1\sin^2\varphi_1 + K_{u2}d_2\sin^2\varphi_2 - H[d_1M_1\cos(\varphi_H - \varphi_1) + d_2M_2\cos(\varphi_H - \varphi_2)] + J_1\cos(\varphi_1 - \varphi_2) + J_2\cos^2(\varphi_1 - \varphi_2), \tag{2}$$

where K_{u1} and K_{u2} are the uniaxial anisotropy constants, φ_H is the angle between H and the easy axis of the SAF (i.e., the y axis), M_1 and M_2 are the saturation magnetizations of the two FM layers, d_1 and d_2 are their thicknesses, and J_1 and J_2 are the bilinear and biquadratic exchange coupling constants [23]. A positive J_1 favors antiparallel coupling [24], leading to a SAF structure. The biquadratic coupling constant J_2 is introduced to account for the effect of spacer pinholes and interface roughness [25]. In order to be consistent with the measurement configuration, hereafter we set $\varphi_H = 0$, i.e., we sweep the field along the y axis only. The simulated results for φ_1 and φ_2 as a function of H for both forward (solid lines) and backward (dashed lines) sweeping of the structures are given in Appendix A.

As discussed in detail in Appendix A, depending on the sense of rotation in the layer that starts to rotate first, there are four possible combinations of φ_1 and φ_2 during a complete loop of field sweeping, which leads to different types of field dependence of the terahertz emission, as discussed below.

Based on the simulated φ_1 and φ_2 values given in Appendix A, we can calculate M_y, ΔM_x, and ΔM_y as a function of the external field H. As discussed above, the M_y-H curve corresponds to the M-H loop measured by a vibrating sample magnetometer (VSM), and the $\mp\Delta M_x$-H and $\pm\Delta M_y$-H curves correspond to E_y and E_x of the terahertz wave as a function of H. The calculation results for the Fe-Mn-Pt SAF are shown in Figs. 2(a)–2(d), Figs. 2(e)–2(h), and Figs. 2(i)–2(l) for M_y, ΔM_y, and $-\Delta M_x$, respectively. Each of these sets of curves corresponds to the four sets of φ_1 and φ_2 values described in Appendix A. As can be seen from the figures, the M_y-H and ΔM_y-H curves cannot allow us to tell the difference between the four different types of magnetization reversal process. However, the $-\Delta M_x$-H loops are distinct in the four different cases. As we show later experimentally, this difference serves as a powerful tool to probe the magnetization reversal process in SAF structures. Similar

results are obtained for the Co-Fe-B SAF, as shown in Figs. 3(a)–(d) for M_y, Figs. 3(e)–(h) for $-\Delta M_y$, and Figs. 3(i)–(l) for ΔM_x. As in the case of the Fe-Mn-Pt SAF, there is no difference between the four different cases for M_y and ΔM_y, but there is a clear difference in ΔM_x. Since the absolute polarity of the terahertz emission can be obtained from control samples with a single-layer FM, the four types of magnetization reversal process can be unambiguously distinguished by the polarity of E_y of the terahertz wave.

III. EXPERIMENTAL DETAILS

The samples investigated in this study are listed in Table I. All the samples are deposited on 500-μm-thick fused-quartz substrates using dc magnetron sputtering with base and working pressures of 2×10^{-8} and 3×10^{-3} Torr, respectively. The Fe-Mn-Pt films are prepared by cosputtering of $Fe_{0.8}Mn_{0.2}$ and Pt targets. The chemical composition of all the samples is determined by x-ray photoelectron spectroscopy [26]. With $Fe_{80}Mn_{20}$ and Pt cathode powers of 50 and 15 W, respectively, we are able to produce a $(Fe_{0.8}Mn_{0.2})_{0.67}Pt_{0.33}$ film with an anomalous Hall angle of $\theta_{AH} = 0.0269$, which is comparable to the spin Hall
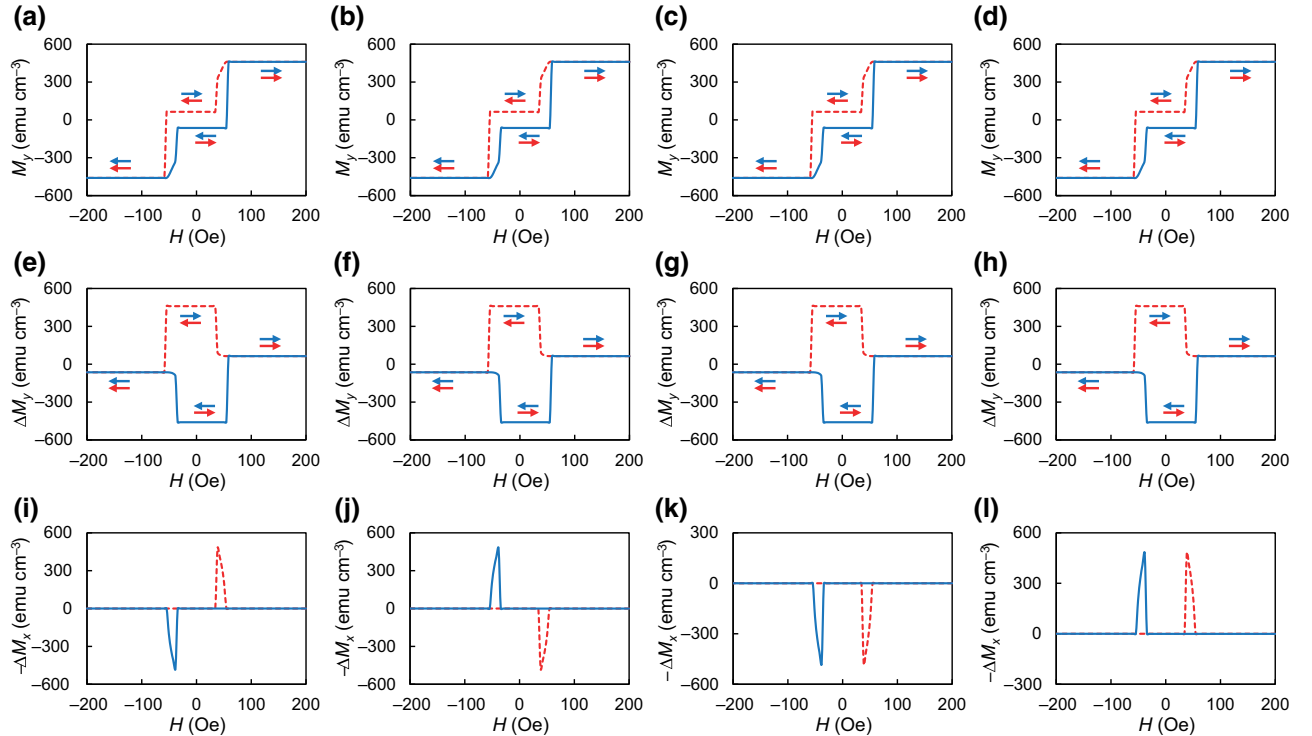

FIG. 2.   Simulated longitudinal (along y axis) and transverse (along x axis) components of total (i.e., $\mathbf{M} = \mathbf{M}_1 + \mathbf{M}_2$) and differential (i.e., $\Delta\mathbf{M} = \mathbf{M}_1 - \mathbf{M}_2$) components of the magnetization of a Fe-Mn-Pt SAF versus a sweeping external field (H). (a)–(d), $M_y = M_{y1} + M_{y2}$; (e)–(h), $\Delta M_y = M_{y1} - M_{y2}$; (i)–(l), $-\Delta M_x = M_{x2} - M_{x1}$. The four different cases in each row correspond to the four different combinations of rotation directions of $\mathbf{M}_1$ and $\mathbf{M}_2$ when the SAF is subjected to the sweeping field, as detailed in Appendix A. The solid and dashed lines represent forward and backward sweeping, respectively. The blue and red arrows indicate the directions of $\mathbf{M}_1$ and $\mathbf{M}_2$ (right, $+y$ direction; left, $-y$ direction).
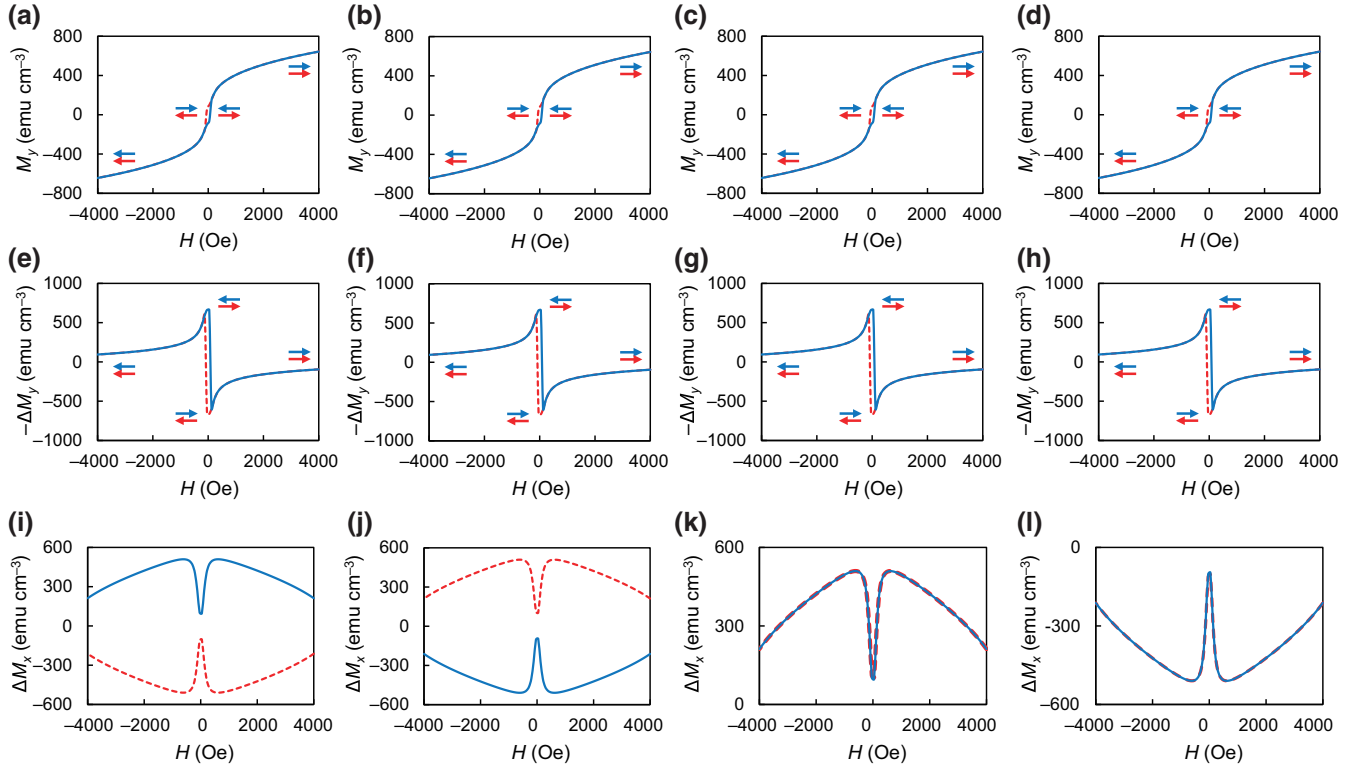
FIG. 3.   Simulated longitudinal (along y axis) and transverse (along x axis) components of total (i.e., $\mathbf{M} = \mathbf{M}_1 + \mathbf{M}_2$) and differential (i.e., $\Delta\mathbf{M} = \mathbf{M}_1 - \mathbf{M}_2$) components of the magnetization of a Co-Fe-B SAF versus a sweeping external field (H). (a)–(d), $M_y = M_{y1} + M_{y2}$; (e)–(h), $-\Delta M_y = M_{y2} - M_{y1}$; (i)–(l), $\Delta M_x = M_{x1} - M_{x2}$. The four different cases in each row correspond to the four different combinations of rotation directions of $\mathbf{M}_1$ and $\mathbf{M}_2$ when the SAF is subjected to the sweeping field, as detailed in Appendix A. The solid and dashed lines represent forward and backward sweeping, respectively. The blue and red arrows indicate the directions of $\mathbf{M}_1$ and $\mathbf{M}_2$ (right, $+y$ direction; left, $-y$ direction).

angle of Pt [26]. For simplicity, hereafter we refer to $(Fe_{0.8}Mn_{0.2})_{0.67}Pt_{0.33}$ as Fe-Mn-Pt unless otherwise specified. A 4-nm MgO capping layer is deposited on top of the Fe-Mn-Pt to prevent oxidation [27]. As discussed above, it also functions as a reflective layer for superdiffusive electrons. The Co-Fe-B is deposited from a single target of $Co_{20}Fe_{60}B_{20}$. A standard terahertz emission spectroscopy system is used for generation and detection of terahertz waves from the various samples. The system is driven by a femtosecond Ti:sapphire laser with a pulse width of 35 fs, a repetition rate of 1 kHz, a wavelength of 800 nm, and an excitation laser power of 120 mW (equivalent to a fluence of 330 $\mu J/cm^2$). During the field-sweeping measurement, an in-plane magnetic field is applied in the easy-axis direction using an electromagnet. In our particular measurement configuration, the easy axis is aligned along the y axis, and the z axis is the laser-beam and terahertz-wave propagation direction. The terahertz emission is calibrated [28] and detected using electro-optical (EO) sampling with a 1000-μm-thick ZnTe detector with a $\langle 110 \rangle$ crystalline orientation; the magnitudes in all figures indicate the EO signal acquired by the detector when balanced. All measurements are performed in a dry nitrogen-gas environment. The magnetometry measurements are carried out using a Quantum Design VersaLab system.

TABLE I.   Samples used in this study. The numbers in brackets denote the thickness in nanometers. "Fe-Mn-Pt" and "Co-Fe-B" refer to $(Fe_{0.8}Mn_{0.2})_{0.67}Pt_{0.33}$ and $Co_{20}Fe_{60}B_{20}$, respectively.

Sample name	Sample structure
Fe-Mn-Pt SAF	Quartz/Fe-Mn-Pt(4 nm)/Ru(0.8 nm)/Fe-Mn-Pt(4 nm)/MgO(4 nm)
Co-Fe-B SAF	Quartz/Pt(2 nm)/Co-Fe-B(4 nm)/Ru(0.8 nm)/Co-Fe-B(3 nm)/Pt(2 nm)/MgO(4 nm)
Fe-Mn-Pt single layer	Quartz/Fe-Mn-Pt(5 nm)/MgO(4 nm)
Co-Fe-B/Pt bilayer	Quartz/Co-Fe-B(3 nm)/Pt(3 nm)/MgO(4 nm)

IV. RESULTS AND DISCUSSION

A. Magnetic properties of Fe-Mn-Pt and Co-Fe-B SAFs

We first study the magnetic properties of the Fe-Mn-Pt and Co-Fe-B SAFs obtained using a VSM with a magnetic field applied parallel to the easy-axis direction. Figure 4(a) shows the *M-H* curves of five Fe-Mn-Pt SAFs with the structure quartz/Fe-Mn-Pt(d_1)/Ru(0.8 nm)/Fe-Mn-Pt(d_2)/MgO(4 nm). The curves are shifted vertically for clarity. For simplicity, we use (d_1, d_2) to indicate the thickness combination (in nanometers) of the two Fe-Mn-Pt layers in the SAF. Except for the (3, 2) sample, all other SAFs exhibit an antiparallel state of $\mathbf{M}_1$ and $\mathbf{M}_2$ at small fields. In what follows, we take the (9, 3) sample as an example to explain briefly how the magnetizations respond to a sweeping external field. In order to be consistent with the simulation results discussed above, we begin with the backward sweeping process first. In the initial stage, both $\mathbf{M}_1$ and $\mathbf{M}_2$ are aligned along the $+y$ direction. The net magnetization in the field direction is $M_1 + M_2$. When the field strength is gradually reduced from 200 Oe, $\mathbf{M}_2$ is reversed at around 95 Oe due to the negative exchange-coupling field. This leads to recovery of the first antiferromagnetic (AF) state, with a net magnetization of $M_1 - M_2$. The AF state is maintained until the field is reduced to zero and then changes its direction. Upon a further increase in the field strength in the negative direction, $\mathbf{M}_1$ starts to rotate in the opposite direction at -8 Oe due to Zeeman-energy gain, and the magnetization reversal process is completed at about 24 Oe. This induces a simultaneous flip of $\mathbf{M}_2$ back to the $+y$ direction, thereby leading to the second AF state, with a net magnetization of $M_2 - M_1$. When the field strength is further increased in the negative direction to -95 Oe, both $\mathbf{M}_1$ and $\mathbf{M}_2$ are aligned along the $-y$ direction, which gives a net magnetization of $-M_1 - M_2$. The reversals of magnetization take place

during forward sweeping from -200 to 200 Oe. The reversals of magnetization in the (5, 3) and (4, 3) samples are essentially the same as those in the (9, 3) sample except that the field at which $\mathbf{M}_2$ reverses becomes smaller, and the net magnetization also changes more gradually with the external field due to the rotation of $\mathbf{M}_1$ as well. However, a clear difference is seen in the *M-H* loop of the (4, 4) sample. Unlike the case for other three samples, $\mathbf{M}_2$ stays in the $-y$ direction after it is switched at a positive field. The flipping of $\mathbf{M}_2$ to the $+y$ direction does not happen at a negative field, because it does not result in a significant Zeeman-energy gain from simply switching the directions of $\mathbf{M}_1$ and $\mathbf{M}_2$ when the difference between $M_1 d_1$ and $M_2 d_2$ is small. Note that although the two FM layers have the same thickness in the (4, 4) sample, their magnetization and thickness products are slightly different due to the fact that the two layers are deposited on different materials, one directly on the quartz substrate and the other one on the Ru layer. For the sake of simplicity, we assume that the actual thickness is the same as the nominal thickness, and that the difference between $M_1 d_1$ and $M_2 d_2$ is mainly due to the difference in magnetization. This gives saturation magnetizations of $M_1 = 262$ emu/cm³ and $M_2 = 198$ emu/cm³. These values are used in the simulation. As can be seen, the *M-H* loop obtained from the VSM measurement is in good agreement with the simulation results shown in Fig. 2(a). In addition, we also measure the *M-H* loops of the (4, 4) sample at elevated temperatures from 300 to 400 K, and the results are shown in Fig. 4(b). The *M-H* loops at different temperatures are quantitatively the same, though the switching field becomes smaller and the switch itself also becomes sharper when the temperature increases. This is presumably caused by the decrease in both the exchange constant and the uniaxial anisotropy of the Fe-Mn-Pt layers induced by temperature. Despite this, the SAF state is maintained even at temperatures up to 400 K.
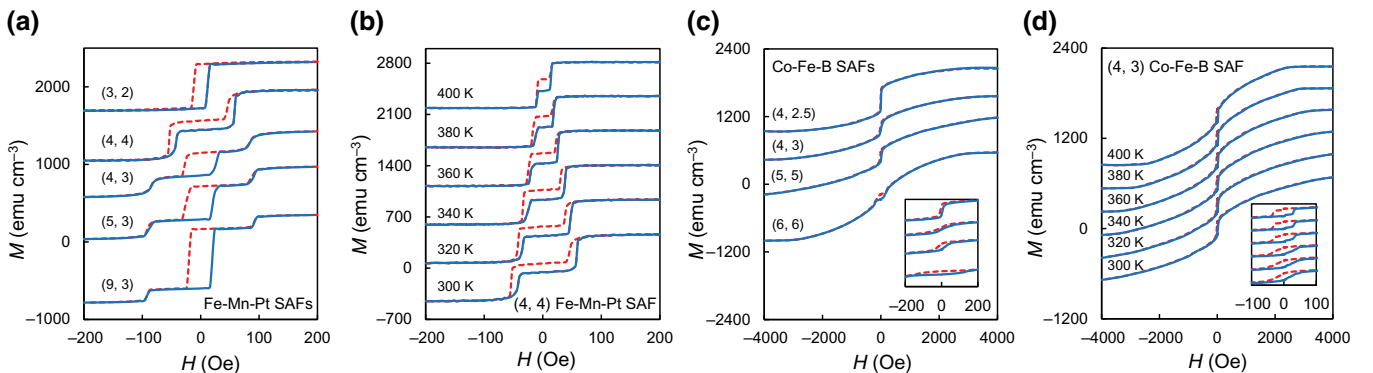

FIG. 4.   Magnetic properties of the SAFs. The solid lines represent forward sweeping, and the dashed lines represent backward sweeping. (a) *M-H* curves of the (d_1, d_2) Fe-Mn-Pt SAFs. (b) Temperature dependence of the *M-H* loop of the (4, 4) Fe-Mn-Pt SAF. (c) *M-H* curves of the (d_1, d_2) Co-Fe-B SAFs. Inset: *M-H* curves in the field region from -200 Oe to 200 Oe. (d) Temperature dependence of the *M-H* loops of the (4, 3) Co-Fe-B SAF. Inset: *M-H* curves in the field region from -100 Oe to 100 Oe.

The *M-H* loops for the four Co-Fe-B SAFs with thickness combinations of (6, 6), (5, 5), (4, 3), and (4, 2.5) are shown in Fig. 4(c). The inset is an enlarged portion of the low-field region. As discussed in Sec. II, the large J_1 and J_2 values result in a more gradual rotation of $\mathbf{M}_1$ and $\mathbf{M}_2$ compared with the Fe-Mn-Pt SAFs. The experimental *M-H* loops are in qualitative agreement with the simulated ones shown in Figs. 3(a)–3(d). As shown in the inset, among the four samples, the (4, 3) sample gives the smallest net moment at zero field, and therefore, in both the simulation and the terahertz measurements, we focus on this sample. As can be seen, a field of up to 4000 Oe is required to saturate $\mathbf{M}_1$ and $\mathbf{M}_2$ in the $+y$ direction. During backward sweeping, when the magnetic field decreases from 4000 Oe, $\mathbf{M}_1$ and $\mathbf{M}_2$ start to rotate gradually in opposite directions, leading to a gradual decrease of the magnetization from 680 emu/cm^3 at 4000 Oe to 80 emu/cm^3 at 100 Oe. At this field, $\mathbf{M}_2$ is nearly reversed, whereas $\mathbf{M}_1$ goes back to the original saturation direction along the $+y$ axis. This corresponds to the first AF state, from which we can infer that $M_1 = 380$ emu/cm^3 and $M_2 = 300$ emu/cm^3, assuming the actual thickness is the same as the nominal thickness. Shortly after the field is reversed, we reach the second AF state, in which both $\mathbf{M}_1$ and $\mathbf{M}_2$ switch their directions, after which both gradually rotate and saturate along the $-y$ direction at around -4000 Oe. The forward sweeping shows a similar trend, which eventually leads to the experimentally observed *M-H* loop. Figure 4(d) shows the *M-H* loops for the same sample at temperatures from 300 to 400 K. Again, the inset shows an enlarged view of the low-field region. When the temperature increases, it becomes easier to saturate the magnetization in both field directions due to the decrease of the exchange constant (4000 Oe at 300 K versus 2430 Oe at 400 K). In the meantime, the field range for the AF state also becomes narrower. As in the case of the (4, 4) Fe-Mn-Pt

sample, the (4, 3) Co-Fe-B sample also maintains its SAF configuration at 400 K. This ensures that the sample can withstand the heating effect, if any, of the laser irradiation during the terahertz measurement.

B. Terahertz emission of Fe-Mn-Pt and Co-Fe-B SAFs

We now turn to the terahertz emission from the (4, 4) Fe-Mn-Pt and (4, 3) Co-Fe-B SAFs. The terahertz generation mechanism for the Fe-Mn-Pt SAF is discussed in detail in Appendix B. As for the Co-Fe-B SAF, with Pt layers on both sides, we assume that the ISHE mechanism developed for a bilayer emitter applies directly to a SAF as well. Figure 5(a) shows the terahertz time-domain waveforms for the (4, 4) Fe-Mn-Pt sample at an applied field of 0 (dashed line) and 200 Oe (solid line). The laser fluence is 330 μJ/cm^2. For comparison, we also show the result for a single-layer Fe-Mn-Pt emitter with a thickness of 5 nm (dotted line) measured under the same conditions. It should be pointed out that the time-domain waveforms shown in Figs. 5(a) and 5(b) are normalized by the laser fluence. The peak-amplitude ratios are as follows: $E_{\text{SAF(0Oe)}}/E_{\text{SAF(200Oe)}} = 3.99$ and $E_{\text{SAF(200Oe)}}/E_{\text{Fe-Mn-Pt}} = 0.55$. As we have demonstrated previously [19], in the case of a Fe-Mn-Pt single-layer emitter, the terahertz amplitude is determined by the net longitudinal superdiffusive current $j_l = j_{l1} - j_{l2}$, where j_{l1} and j_{l2} are the backflow spin-polarized currents from the two interfaces, one with the substrate and the other with the MgO capping layer. We also show that the terahertz emission is strongly dependent on the Fe-Mn-Pt thickness. The Fe-Mn-Pt SAF shown in Fig. 1(a) has four interfaces: (i) quartz/Fe-Mn-Pt, (ii) Fe-Mn-Pt/Ru, (iii) Ru/Fe-Mn-Pt, and (iv) Fe-Mn-Pt/MgO. Since both the Fe-Mn-Pt and Ru are metallic layers, we may assume that the backflow cur-
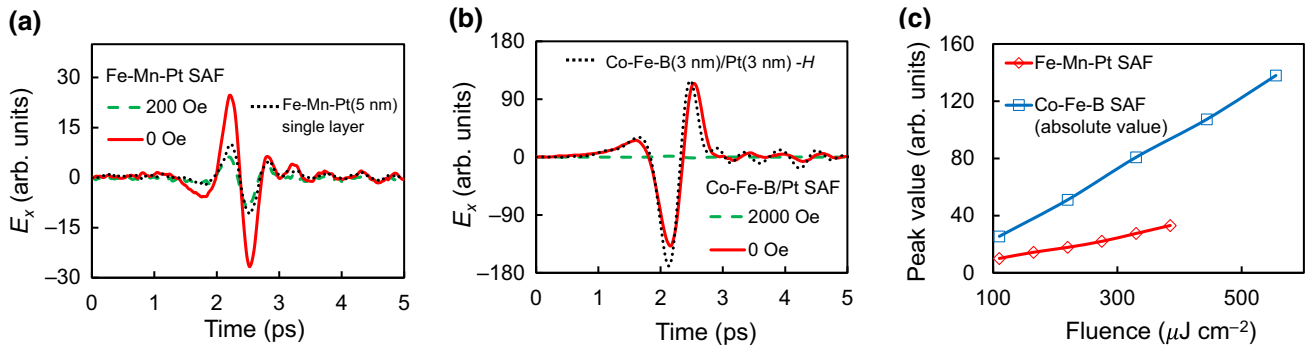
FIG. 5.   Time-domain terahertz emission waveforms from the SAF structures. (a) Terahertz waveforms from the (4, 4) Fe-Mn-Pt SAF at 200 Oe (dashed line) and 0 Oe (solid line), and from a Fe-Mn-Pt(5 nm) single-layer emitter (dotted line) at a positive magnetic field. (b) Terahertz waveforms from the (4, 3) Co-Fe-B SAF at 2000 Oe (dashed line) and 0 Oe (solid line), and from a Co-Fe-B(3 nm)/Pt(3 nm) bilayer emitter (dotted line) at a negative magnetic field. (c) Pump-fluence dependence of the terahertz peak amplitude for the Fe-Mn-Pt (diamonds) and Co-Fe-B (squares) SAFs.

rents from interfaces (ii) and (iii) are much smaller than those from the interfaces with MgO and the substrate. This is a reasonable assumption considering the polycrystalline nature of the sample, although further studies are required to quantify the reflection at the metallic interfaces [29]. Therefore, at 200 Oe, the SAF may be treated as a single-layer emitter with an equivalent thickness of 8.8 nm. As shown in Ref. [19], for a single-layer Fe-Mn-Pt emitter, the terahertz emission amplitude for a thickness of 8.8 nm is about 60% of that for 5 nm. This explains well the $E_{\text{SAF(200Oe)}}/E_{\text{Fe-Mn-Pt}}$ ratio of 0.55. On the other hand, at zero field, i.e., when the two FMs are antiparallel, the contributions from the quartz/Fe-Mn-Pt and Fe-Mn-Pt/MgO interfaces add up instead of cancelling each other out. Therefore, as a simple estimation, the $E_{\text{SAF(0Oe)}}/E_{\text{SAF(200Oe)}}$ ratio may be approximated as $(1 + \alpha)/(1 - \alpha)$, where α is the ratio between the backflow currents from the MgO and quartz interfaces. For a $E_{\text{SAF(0Oe)}}/E_{\text{SAF(200Oe)}}$ ratio of 3.99, α turns out to be 0.6. The difference between the top and bottom interfaces is not as large as what we found previously in the case of single emitters. This is presumably caused by the insertion of a thin Ru layer, which helps to reduce the roughness of the Fe-Mn-Pt/MgO interface. This is a desirable result, as it significantly enhances the terahertz emission in the AF state. These results further affirm the AHE origin of the terahertz emission as proposed in our previous study.

A similar response to the external field is observed in the terahertz emission from the Co-Fe-B SAF except that the polarization is opposite to that of the Fe-Mn-Pt SAF. Figure 5(b) shows the terahertz waveforms from the (4, 3) Co-Fe-B SAF at 0 Oe and 2000 Oe. Also shown is the terahertz waveform from the Co-Fe-B(3 nm)/Pt(3 nm) bilayer control sample with a negative applied field. Similarly to the case of the Fe-Mn-Pt SAF, the terahertz emission amplitude is maximum at 0 Oe but nearly zero at the saturation field. The opposite polarity at zero field can be understood as follows. When the pumping directions are the same, i.e., both are from the substrate side as shown in Fig. 1, the terahertz polarization of the Fe-Mn-Pt SAF follows the sign of $\mathbf{M}_1$, assuming $j_{l1} > j_{l2}$. Note that whether the polarization is positive or negative is relative, and it is calibrated using the single-layer sample. We have previously demonstrated that the anomalous Hall angle of Fe-Mn-Pt and the spin Hall angle of Pt have the same sign [26]. Therefore, in the same measurement configuration, the terahertz polarization of the Co-Fe-B SAF should follow the sign of $\mathbf{M}_2$. The opposite polarity in Fig. 5(b) is obtained by first saturating the sample in the $+y$ direction and then reducing the field to zero. In this case, the sample is in the first AF state, i.e., $\mathbf{M}_1$ is in the $+y$ and $\mathbf{M}_2$ in the $-y$ direction. Although it is not shown here, we verify that the polarization is opposite if we first saturate the sample using a large negative field and then reduce the field to zero. This explains why the polarity is opposite for the two

samples. As can be seen in Fig. 5(b), the amplitude for the (4, 3) Co-Fe-B SAF sample at zero field (solid line) is about 82% of that for the Co-Fe-B(3 nm)/Pt(3 nm) bilayer sample (dotted line). But this does not mean that there is no enhancement of terahertz emission in the SAF sample. As demonstrated by previous studies, the terahertz emission of FM/HM bilayers is strongly dependent on the individual layers as well as on the total thickness. The total thickness of the (4, 3) Co-Fe-B SAF sample is 11.8 nm, almost double of that the Co-Fe-B(3 nm)/Pt(3 nm) bilayer sample. If we treat the SAF sample equivalently as a bilayer sample with a total thickness of 11.8 nm, the estimated peak amplitude is 37% of that for the bilayer sample [2,30]. The fact that the peak amplitude for the SAF sample at zero field is 82% of that for the bilayer sample implies that the terahertz signal from the SAF sample indeed is the sum of contributions from the two FM layers at zero field. We also investigate the pumping-fluence dependence of the results from the SAF samples, and the results are shown in Fig. 5(c). In order to avoid damaging the samples, we increase the laser fluence to only 385 μJ/cm^2 for the Fe-Mn-Pt SAF, and for the Co-Fe-B SAF, we increase it to 550 μJ/cm^2. Both samples show a linear increase with the pumping fluence, indicating that although laser heating increases the sample temperature, it does not affect the terahertz emission obviously in this fluence range. The large thickness makes the SAF samples relatively more insensitive to heating effects, which is potentially an advantage of a SAF emitter compared with a single-layer or bilayer emitter when it comes to practical applications.

C. Field dependence of terahertz emission from Fe-Mn-Pt and Co-Fe-B SAFs

As demonstrated by the simulation results presented in Sec. II, terahertz emission provides a convenient tool to study the magnetization reversal process of SAF structures. In order to see how the two magnetic layers rotate during field sweeping, we fix the time at the first peak of the terahertz waveform and investigate how the peak amplitude varies with the external field. We perform measurements at different delay times either before or after the peak position. The shape of the terahertz-H loop looks almost the same except for the amplitude, suggesting that magnetic dipole radiation has a negligible effect on the terahertz-H loop due to its small contribution [19]. Figure 6(a) shows the peak value of the terahertz E_x component for the (4, 4) Fe-Mn-Pt SAF versus the applied magnetic field for laser fluences from 110 to 385 μJ/cm^2. The solid (dashed) line corresponds to forward (backward) sweeping of the magnetic field. The overall shape of the E_x-H curve agrees well with the simulated ΔM_y-H curves shown in Figs. 2(e)–2(h). When the external field is large, both $\mathbf{M}_1$ and $\mathbf{M}_2$ are aligned with the field direction, resulting in a
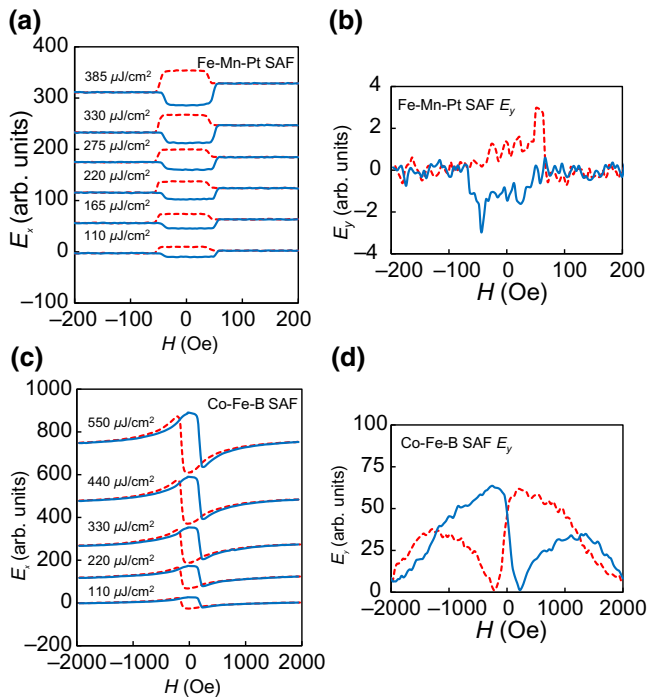
FIG. 6. Magnetic field dependence of the terahertz emission. The solid lines represent forward sweeping, and the dashed lines represent backward sweeping. (a) E_x-H curve for the (4, 4) Fe-Mn-Pt SAF at pumping fluences from 110 to 385 $\mu J/cm^2$; (b) E_y-H curve for the (4, 4) Fe-Mn-Pt SAF at a pumping fluence of 330 $\mu J/cm^2$; (c) E_x-H curve for the (4, 3) Co-Fe-B SAF at fluences from 110 to 550 $\mu J/cm^2$; (d) E_y-H curve for the (4, 3) Co-Fe-B SAF at a pumping fluence of 330 $\mu J/cm^2$.

small residual emission (negative when $H < 0$ and positive when $H > 0$). When H is within the range ± 39 Oe, the terahertz amplitude is maximum due to the antiparallel alignment of $\mathbf{M}_1$ and $\mathbf{M}_2$. The two AF states produce terahertz emission of the same amplitude but opposite polarization. When the laser fluence is increased from 110 to 385 $\mu J/cm^2$, although the amplitude increases almost linearly, the shape remains almost unchanged; the width of the central region does not show an obvious narrowing trend, which is different from the temperature-dependence results, meaning that an increase in the laser fluence up to 385 $\mu J/cm^2$ does not cause an additional heating effect. This corresponds well with the linear increase of the terahertz peak amplitude shown in Fig. 5(c). As discussed in Sec. II, the E_x component of the terahertz emission is unable to probe the directions of $\mathbf{M}_1$ and $\mathbf{M}_2$ during the magnetization reversal process. To this end, we measure the field dependence of the E_y component by rotating both the analyzer and the detector by 90°. Compared with the E_x component, it is more challenging to the measure the E_y component for the Fe-Mn-Pt SAF. This is because the reversal of the magnetization of the two layers occurs in a narrow magnetic field range (approximately 24 Oe), and

the E_y signal is much weaker than E_x. To mitigate the situation, we repeat the measurements 30 times, and Fig. 6(b) shows the averaged signal. For this particular measurement, the laser fluence is 330 $\mu J/cm^2$. As expected, there is a sharp peak near the switching region during both backward and forward sweeping. The squarelike hysteresis loop at low field may be caused by a slight misalignment of the easy axis with the external field (by approximately 1°). The measurement starts with backward sweeping. At 200 Oe, both $\mathbf{M}_1$ and $\mathbf{M}_2$ are aligned in the $+y$ direction, and therefore there is no E_y component detected. When the field decreases to around 60 Oe, both $\mathbf{M}_1$ and $\mathbf{M}_2$ start to rotate away from the y axis, leading to a nonzero net projection of the magnetization in the x direction, thereby giving rise to a sharp E_y peak. The sign of E_y during field sweeping is similar to the simulated result for $-\Delta M_x$ in Fig. 2(i), where a positive (negative) peak appears during backward (forward) sweeping. Therefore, the E_y-H curve unambiguously determines the rotation direction of the magnetization, i.e., $\mathbf{M}_1$ rotates clockwise, whereas $\mathbf{M}_2$ rotates counterclockwise, during both forward and backward sweeping for this particular sample. Now the question is: what determines the rotation direction given the fact that, from an energetic point of view, there is no difference between clockwise and counterclockwise rotation? Theoretically, this is indeed the case. However, during an actual measurement, there is always the possibility of misalignment between the external-field direction and the easy-axis direction of the sample. When such a misalignment is present, the layer with the larger magnetization should deviate less from the field direction so as to minimize the Zeeman energy. This will set a preferred rotation direction for the layer with the larger magnetization. Once this is set, the other layer will rotate in the opposite direction to minimize the exchange energy. This explains why the particular E_y-H curve shown in Fig. 6(b) is obtained.

We now turn to the Co-Fe-B SAF sample. Figure 6(c) shows the peak value of the terahertz E_x component for the (4, 3) Co-Fe-B SAF versus the applied magnetic field for laser fluences from 110 to 550 $\mu J/cm^2$. The solid (dashed) lines correspond to forward (backward) sweeping of the magnetic field. Again, the terahertz emission does not change much with the pumping fluence except for the peak amplitude. The overall shape of the E_x-H curve agrees well with the simulated $-\Delta M_y$-H curves shown in Figs. 3(e)–3(h). The gradual change of the terahertz emission with the external field is in good agreement with the VSM results, although the saturation field is smaller in the terahertz measurement. This is presumably caused by a laser-heating-induced reduction of the exchange constant, as also observed in the Fe-Mn-Pt sample. Now we explain briefly the $-\Delta M_y$-H curve by focusing on the measurement done at a fluence of 330 $\mu J/cm^2$. We can see that the terahertz amplitude gradually increases in the negative direction when the field is reduced from 2000 Oe. This is

because $\mathbf{M}_1$ and $\mathbf{M}_2$ start to rotate away from the $+y$ axis in opposite directions. Since $M_2 d_2$ is smaller than $M_1 d_1$, $\mathbf{M}_2$ rotates faster than $\mathbf{M}_1$ with respect to the field change. When the angle between $\mathbf{M}_2$ and the $+y$ axis reaches a critical value, $\mathbf{M}_1$ starts to rotate back to $+y$. This increases further the speed at which $\mathbf{M}_2$ approaches the $-y$ direction. Therefore, E_x keeps increasing in the negative direction until it reaches its negative maximum. When the field reverses its direction and increases in strength, it is energetically more favorable to align $\mathbf{M}_1$ with the external field, as $M_1 d_1 > M_2 d_2$. This forces $\mathbf{M}_2$ to rotate back to the $+y$ direction, and at the same time $\mathbf{M}_1$ rotates to the $-y$ direction. As a result, E_x starts to increase at around -80 Oe and reaches a positive maximum at -250 Oe. From -250 to -2000 Oe, the terahertz emission gradually decreases to zero due to the gradual alignment of the two magnetic layers with the external field. The forward-sweeping curve can be understood in the same way. As with the case of the Fe-Mn-Pt SAF, to probe the rotation directions of $\mathbf{M}_1$ and $\mathbf{M}_2$, we have to measure the E_y component. The field-sweeping measurement results for E_y are shown in Fig. 6(d). Unlike the case of the Fe-Mn-Pt SAF, E_y always maintains the same sign during both backward and forward sweeping. The minima of E_y at positive and negative fields correspond to the maxima of E_x at positive and negative fields during forward and backward sweeping. Apart from a slightly larger hysteresis, the measured E_y-H relation resembles well the simulated results in Fig. 3(k). This suggests that, instead of rotating by one cycle in the same sense of rotation, i.e., either clockwise or counterclockwise, during the backward and forward sweeping, both $\mathbf{M}_1$ and $\mathbf{M}_2$ rotate back when the sweeping direction is reversed. This is so because in the terahertz measurement, even at a field of 2000 Oe (limited by the electromagnet used in the setup), we are unable to saturate the magnetization of the Co-Fe-B layers. This explains the difference between the Fe-Mn-Pt and Co-Fe-B SAF samples. Again, the initial rotation directions of $\mathbf{M}_1$ and $\mathbf{M}_2$ when the field is reduced from 2000 Oe are set by the misalignment angle between the applied field and the easy axis.

D. Discussion

As demonstrated above both theoretically and experimentally, by measuring the E_x and E_y components of the terahertz emission, we are able to determine the rotation directions of $\mathbf{M}_1$ and $\mathbf{M}_2$ unambiguously, which is not possible through standard magnetometry measurements. Apparently, the terahertz signal is more informative than the net moment because (i) it is a vector that can be used to map out the magnetization direction of each layer, and (ii) it is even more sensitive when $M_1 d_1 \approx M_2 d_2$. It is worth pointing out that, as long as one is concerned with the in-plane magnetization of an individual SAF layer, the terahertz-based technique is superior to other commonly

used magnetic characterization techniques that are able to probe magnetization reversal processes, such as the magneto-optic Kerr effect (MOKE) and x-ray magnetic circular dichroism (XMCD). The key difference is that in both the MOKE and the XMCD technique, the light propagation and polarization directions are the same for the two layers. In contrast, in the case of terahertz measurements, although the direct excitation source is the pump laser, the laser beam is not really the probe beam *per se*. The actual probe beams are the two superdiffusive currents, with opposite directions. This is equivalent to a MOKE measurement where two laser beams with different polarization directions irradiate the two FM layers of a SAF structure at the same time, which is obviously very difficult to achieve. An alternative way is to measure the longitudinal and transverse magnetization components separately by reconfiguring the MOKE optics, but this would increase the complexity of the measurement system. Even if this is possible, another difficult situation for the MOKE technique is when the signals from the two FM layers have the same magnitude but opposite signs. As the net signal is zero in this case, it is impossible to determine the individual magnetization directions. Nevertheless, we see that the combination of terahertz and MOKE measurements provides a powerful tool to probe the magnetization dynamics of magnetic multilayers, as these techniques are largely complementary to each other. On the other hand, although XMCD has additional elemental selectivity, it still cannot differentiate between $\mathbf{M}_1$ and $\mathbf{M}_2$ if the two layers consist of the same type of material, as in the present case. The only disadvantage of the terahertz-based technique at the moment is its inability to probe the vertical component, which requires further investigations.

V. CONCLUSIONS

In summary, we demonstrate terahertz emission from exchange-coupled SAF structures based on both the AHE and the ISHE. In addition to an enhancement of the terahertz emission, we show both theoretically and experimentally that terahertz emission is a powerful tool to probe magnetization reversal processes in SAF structures. This is possible because the terahertz emission from a SAF structure is proportional to the vector difference of the two magnetizations, $\mathbf{M}_1 - \mathbf{M}_2$, rather than the longitudinal component of $\mathbf{M}_1 + \mathbf{M}_2$. The unique capability of terahertz emission as a magnetization-probing tool comes from the fact that the excitation laser generates two secondary probes, which are superdiffusive currents with opposite directions. The separate secondary probes for each layer give the use of terahertz emission unparalleled advantages over other conventional magnetization-probing techniques such as the MOKE and XMCD techniques.

APPENDIX A: MACROSPIN SIMULATION OF SAF

We conduct a macrospin simulation of Fe-Mn-Pt and Co-Fe-B SAFs based on Eq. (2). Figures 7(a)–7(d) show the simulated results for φ_1 and φ_2 as a function of H for both forward (solid lines) and backward (dashed lines) sweeping of the Fe-Mn-Pt SAF structure. As stated in Sec. II, we adopt the convention that φ_1 and φ_2 are positive for counterclockwise rotation and negative for clockwise rotation; therefore, both 180° and −180° refer to the −y direction, and 360° and −360° are the same as 0°, which is in the +y direction. The parameters used are $M_1 = 262$ emu/cm³, $M_2 = 198$ emu/cm³, $K_{u1} = 4 \times 10^3$ erg/cm³, $K_{u2} = 4 \times 10^3$ erg/cm³, $d_1 = d_2 = 4$ nm, $J_1 = 0.0041$ erg/cm², and $J_2 = 0$. The saturation magnetizations and thicknesses are determined experimentally. The uniaxial anisotropy constants are estimated from the relation $K_{ui} = M_i H_{ki}/2$ ($i = 1$ or 2), where we use the coercivity of the respective layers to approximate the anisotropy field H_k. Once these parameters are known, J_1 can be calculated analytically from the field at which the first reversal occurs in the measured M-H loop of the SAF [31]. The final values of K_{u1}, K_{u2}, and J_1 are optimized by comparing the simulated M-H loop with one measured by a VSM. We find that a reasonably good fitting is obtained when $J_2 = 0$. The magnetizations of the two FM layers are initially aligned antiparallel at zero field. When an external field of adequate strength is applied in the +y direction, the two magnetizations are aligned with the field direction (i.e., $\varphi_1 = \varphi_2 = 0$). When the field strength is gradually reduced, both φ_1 and φ_2 start to deviate from their initial directions. Since $J_1 > 0$, $\mathbf{M}_1$ and $\mathbf{M}_2$ have to rotate in opposite directions. When the external field is perfectly aligned with the easy-axis direction, there is no predetermined preference as to which one will rotate in which direction, and therefore there are two possible senses of rotation for both the forward and the backward sweeping processes, which are summarized in Table II and also illustrated in Figs. 7(i)–7(l). Corresponding to the four scenarios are four sets of φ_1 and φ_2 values, which are shown in Figs. 7(a)–7(d).

We now use Fig. 7(a) as an example to explain how φ_1 and φ_2 vary with the external field, starting from backward sweeping. In this case, both magnetizations are initially aligned in the +y direction, i.e., $\varphi_1 = \varphi_2 = 0$. When the

field strength is reduced, initially both φ_1 and φ_2 remain at 0°. However, when H decreases to 50 Oe, φ_1 (φ_2) becomes negative (positive), with its absolute value gradually increasing as the magnetic field decreases. This means that $\mathbf{M}_1$ starts to rotate away from the y axis in the clockwise direction, whereas $\mathbf{M}_2$ rotates in the counterclockwise direction. When the magnetic field is reduced further, at around $H = 34$ Oe, φ_2 jumps abruptly to 180°, i.e., $\mathbf{M}_2$ reverses its direction. As expected, $\mathbf{M}_1$ rotates back to the +y direction in order to minimize the energy. This is the first AF-coupling state. The AF state is stable until the field reverses its direction and increases its value to $H = -58$ Oe, after which $\mathbf{M}_1$ is aligned with $\mathbf{M}_2$ in the −y direction. The forward sweeping process is exactly the opposite process to backward sweeping. When the field strength is reduced to around $H = -50$ Oe, $\mathbf{M}_1$ ($\mathbf{M}_2$) starts to rotate away from the −y axis in a clockwise (counterclockwise) manner, after which the second AF state is reached in the range −34 Oe < H < 58 Oe, before the magnetizations saturate again in the +y direction. The difference between the first and the second AF state is that, in the two states, $\mathbf{M}_1$ and $\mathbf{M}_2$ point in opposite directions. The processes shown in Fig. 7(b) are exactly the same as those in Fig. 7(a) except that the rotation directions of $\mathbf{M}_1$ and $\mathbf{M}_2$ are swapped. Therefore, after the completion of the backward sweeping process, φ_1 and φ_2 become 180° and −180°, respectively. Figures 7(a) and 7(b) are obtained by assuming that the initial sense of rotation of both φ_1 and φ_2 is the same for both backward and forward sweeping. However, from the point of view of energetics, there is no reason why φ_1 and φ_2 must follow the same sense of rotation during backward and forward sweeping. Therefore, we still have the other two possible reversal processes. Figure 7(c) shows the case where backward sweeping results in the same sense of rotation as in Fig. 7(b), but forward sweeping produces the opposite sense of rotation, i.e., instead of rotating clockwise (counterclockwise) [Fig. 7(j)], φ_1 (φ_2) rotates counterclockwise (clockwise) in the initial stage of magnetization reversal [Fig. 7(k)]. Similarly, Fig. 7(d) corresponds to the case where backward sweeping results in the same sense of rotation as in Fig. 7(a), but forward sweeping has a different result [Fig. 7(l)]. Similar simulations are also conducted for the Co-Fe-B SAF emitters with the parameters $M_1 = 380$ emu/cm³, $M_2 = 300$ emu/cm³, $K_{u1} = 1 \times 10^4$ erg/cm³, $K_{u2} = 7.75 \times 10^3$ erg/cm³, $d_1 = 4$ nm, $d_2 = 3$ nm, $J_1 = 0.122$ erg/cm², and $J_2 = 0.055$ erg/cm². The values of M_1 and M_2 are obtained from the VSM M-H curve, and the values of K_{u1} and K_{u2} are estimated from the coercivity of the corresponding single-layer films. The initial value of J_1 is chosen to be comparable with those reported in other studies [32–34]. J_2 is optimized through simulation. A nonzero value of J_2 after fine tuning is used in order to fit the measured VSM results. Figures 7(e)–7(h) show the simulated φ_1 and φ_2 values as
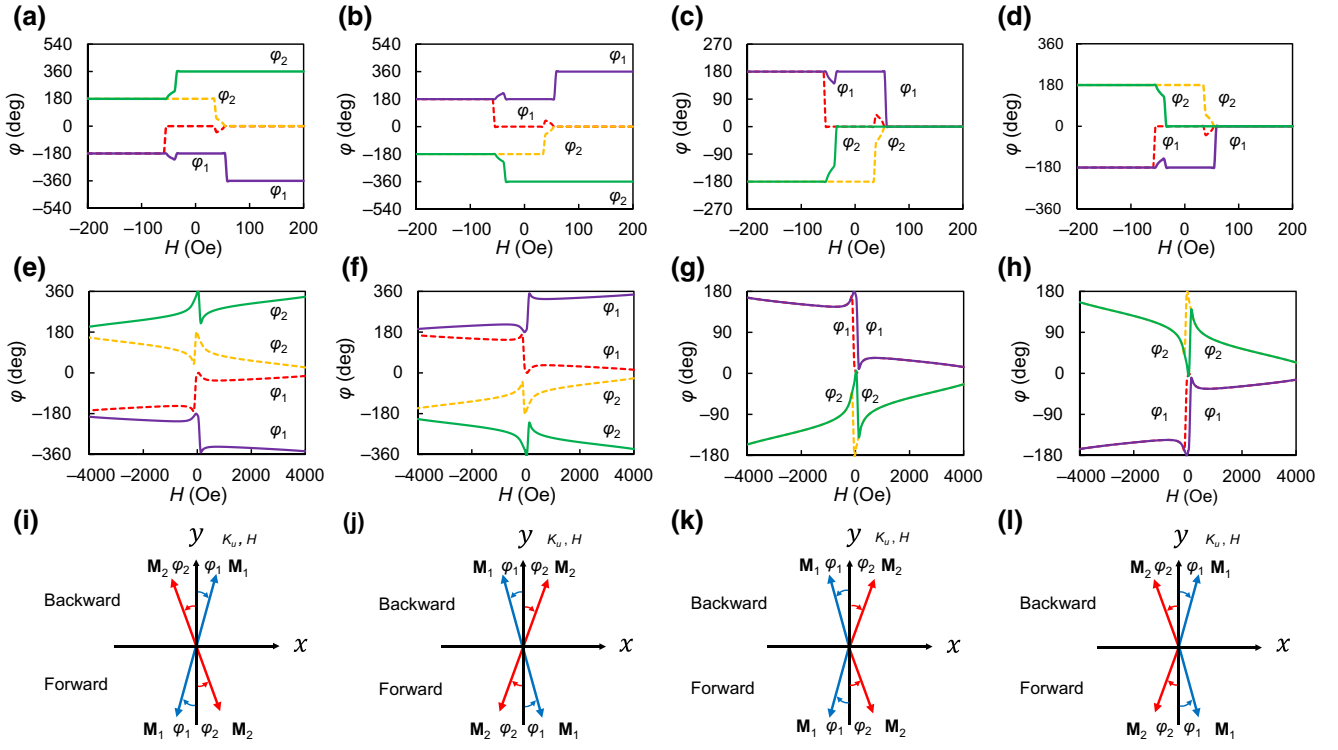
FIG. 7. Simulated φ_1 and φ_2 values for (a)–(d) Fe-Mn-Pt SAF and (e)–(h) Co-Fe-B SAF under a sweeping magnetic field. The four sets of results correspond to the four different combinations of rotation directions of $\mathbf{M}_1$ and $\mathbf{M}_2$ summarized in Table II. φ_1 and φ_2 are positive for counterclockwise rotation and negative for clockwise rotation. The solid lines represent forward sweeping, and the dashed lines represent backward sweeping. (i)–(l) Schematic illustrations of the initial magnetization rotation direction during field sweeping for the four different cases (upper half, backward sweeping; lower half, forward sweeping).

a function of H. The results are qualitatively the same as those for the Fe-Mn-Pt SAF except that there is an additional magnetization-flipping process shortly after the external field changes direction. This is due to the difference in Zeeman energy, which favors the alignment of the FM layer with the larger magnetization in the external-field direction. Besides this, the large J_1 and J_2 values also result in a more gradual rotation of $\mathbf{M}_1$ and $\mathbf{M}_2$ compared with the Fe-Mn-Pt SAF.

APPENDIX B: GENERATION OF SUPERDIFFUSIVE BACKFLOW CURRENTS AND TERAHERTZ EMISSION

As explained in our previous publication [19], when a MgO/FM/quartz trilayer (here, "FM" refers to a metallic ferromagnet) is irradiated by a femtosecond laser,

the electrons are excited to states above the Fermi level in the FM layer [Fig. 8(a)]. Immediately after the excitation, equilibration takes place through two dominant mechanisms, i.e., electron-electron and electron-phonon interactions. Because of the much smaller heat capacity, the electron subsystem quickly reaches a high-temperature (T_e) Fermi-Dirac distribution within 0.1 ps [Fig. 8(b)], whereas the lattice stays close to the ambient temperature (T_p). The electrons subsequently cool and thermalize with their own lattice within a few picoseconds [Fig. 8(c)]. In addition to phonons, magnons also play a role in the equilibration process of hot electrons in ferromagnets. The magnon temperature (T_m) is typically higher than that of the phonons before all three subsystems reach thermal equilibrium [19].

TABLE II. The four different scenarios for the rotation directions of $\mathbf{M}_1$ and $\mathbf{M}_2$ when subjected to an external sweeping field (CW, clockwise; CCW, counterclockwise).

	Scenario I	Scenario II	Scenario III	Scenario IV
Backward sweeping	$\mathbf{M}_1$: CW	$\mathbf{M}_1$: CCW	$\mathbf{M}_1$: CCW	$\mathbf{M}_1$: CW
	$\mathbf{M}_2$: CCW	$\mathbf{M}_2$: CW	$\mathbf{M}_2$: CW	$\mathbf{M}_2$: CCW
Forward sweeping	$\mathbf{M}_1$: CW	$\mathbf{M}_1$: CCW	$\mathbf{M}_1$: CW	$\mathbf{M}_1$: CCW
	$\mathbf{M}_2$: CCW	$\mathbf{M}_2$: CW	$\mathbf{M}_2$: CCW	$\mathbf{M}_2$: CW

Before the electron subsystem reaches equilibrium (i.e., $t < 0.1$ ps), the nonthermal electrons move at a fast speed (approximately 10^6 m/s) in a superdiffusive manner [Fig. 8(d)] [19]. For electrons at a distance of at least a mean free path (λ_e) away from the top interface (e.g., with a MgO capping layer) and bottom interface (e.g., with a quartz substrate), these electrons collide with other electrons to reach thermal equilibrium within the electron subsystem. However, for electrons at a distance shorter than λ_e from the interfaces, they are reflected back to form a backflow current due to reflection at the FM/dielectric interface. The amplitude of the backflow current depends strongly on the material properties and roughness of the interface. For metallic films deposited on a smooth substrate, typically the bottom interface is smoother than the top interface. In this case, the backflow current from the bottom interface (j_{l1}) is larger than that from the top interface (j_{l2}). Therefore, a net longitudinal current is formed in the FM layer, which is subsequently converted to a transverse transient current via the AHE, thereby generating terahertz emission.

(a) Excitation $t = 0$

(b) $T_e \gg T_m > T_p$ $0.1 - 10$ ps

(c) $T_e \approx T_m \approx T_p$ > 10 ps

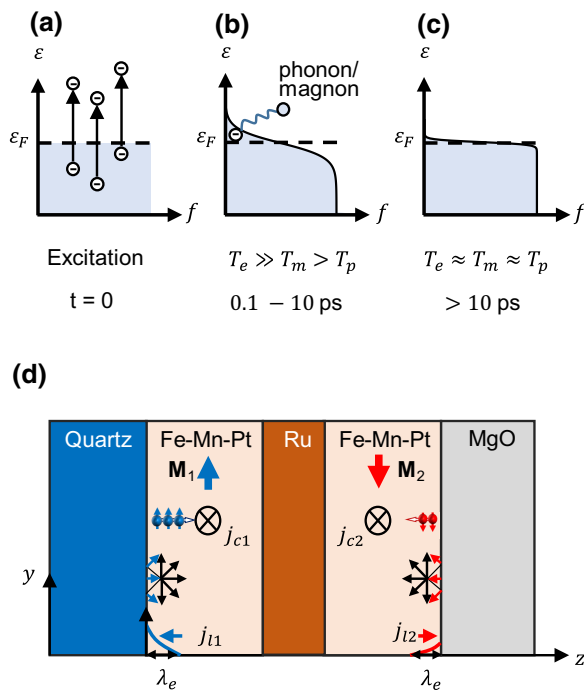**(d)** Quartz | Fe-Mn-Pt $\mathbf{M}_1$ | Ru | Fe-Mn-Pt $\mathbf{M}_2$ | MgO

FIG. 8. (a)–(c) Subprocesses on different time scales after ultrafast laser excitation of a metallic layer. (a) Excitation of nonequilibrium electrons. (b) High-temperature Fermi-Dirac distribution of electron subsystem. (c) Nearly thermal equilibrium state among electrons, phonons, and magnons. (d) Schematic illustration of nonthermal electron reflection at quartz/FM and FM/MgO interfaces, the directions of spin polarity in each Fe-Mn-Pt layer, the formation of backflow currents, and the directions of the charge currents.

The same process is expected to occur in a SAF structure as well. As illustrated in Fig. 8(d), in this case, the backflow currents from the quartz substrate and the MgO capping layer generate a spin-polarized current in $\mathbf{M}_1$ and $\mathbf{M}_2$, respectively. The contribution of the backflow current from the Ru/FM interface is presumably small, considering that both layers are metals. The net longitudinal current in each layer is thus mainly determined by the FM/dielectric interface, and is subsequently converted to terahertz emission via the AHE. This is a reasonable assumption because we have previously estimated that the electron spin diffusion length in Fe-Mn-Pt is around 1.4 nm [19]. In the Fe-Mn-Pt SAF in the present study, the thickness of the individual Fe-Mn-Pt layers is 4 nm, which makes it hard for the backflow spin current to reach and cross the Fe-Mn-Pt/Ru interface. Unlike the single-layer FM case, in which the terahertz emissions due to the backflow currents from the top and bottom interfaces cancel each other partially, here the terahertz emissions from the two layers simply add up due to the antiparallel alignment of the two FM layers at zero field. This is the reason why the SAF structure generates a much stronger terahertz emission for the same equivalent thickness. In addition to the backflow current from the FM/dielectric interface and subsequent terahertz generation via the AHE inside the FM layer, one should also consider the contribution from the backflow current at the FM/Ru interface and the role of Ru as a spin-to-charge converter; however, these are both insignificant, as elaborated on below.

The small reflection of the superdiffusive current at the FM/Ru interfaces also means that the superdiffusive current generated inside each FM layer enters the Ru directly. But, we have enough reason to believe that the currents from the two FM layers mostly cancel out inside the Ru layer due to their opposite directions. Even if they do not completely cancel out, we argue that their effect should be very small. The spin-orbit interaction in Ru is about 3 times smaller than that in Pt [21], and the same relation also holds for the spin Hall angle, which is 0.04 for Ru and approximately 0.11 for Pt [22]. As the amplitude of terahertz emission from FM/NM bilayers is found to be proportional to the spin Hall angle of the NM layer [2], the terahertz emission from the Ru, if any, should be about 3 times smaller than that from the Fe-Mn-Pt layer, as the anomalous Hall angle of Fe-Mn-Pt is comparable to that of Pt (assuming the laser-induced superdiffusive current is the same). Of course, one should be mindful of these values, as even the spin Hall angle for Pt, the best-studied material, varies over a large range. Putting the concrete values aside, experimentally, Zhang *et al.* found that the terahertz emission from a Ru-based heterostructure was much smaller than that from the same structure with Ru replaced by Pd [12]. The two factors combined, i.e., a very small net current and a small spin Hall angle, ensure that

the contribution from the Ru to the terahertz emission can be safely ignored.

Another factor that may affect the terahertz emission is the "spilling over" of the superdiffusive current across the Ru layer so that it enters the other side of the FM. This is in fact a desirable effect for the Fe-Mn-Pt SAF. As we reported previously [19], the terahertz emission in a single-layer FM emitter originates from the backflow current from the top and bottom interfaces. As the reflected currents are always in opposite directions, the contributions from the two surfaces partially cancel each other out, and the net emission is the difference between the two contributions. In order to increase the net emission, we have to increase the difference between the contributions from the two interfaces. This is the reason why, in previous work, we introduced a composition gradient and, in the present work, introduce a SAF structure. The superdiffusive current that enters the Fe-Mn-Pt layer at the other side should be smaller than the backflow current from the FM/oxide interface in a single-layer structure. Therefore, if we divide the SAF into two halves, the terahertz emission from each half should be larger than that of the equivalent single-layer structure. In fact, this is exactly what we observe.

---

[1] T. Kampfrath, M. Battiato, P. Maldonado, G. Eilers, J. Nötzold, S. Mährlein, V. Zbarsky, F. Freimuth, Y. Mokrousov, S. Blügel, M. Wolf, I. Radu, P. M. Oppeneer, and M. Münzenberg, Terahertz spin current pulses controlled by magnetic heterostructures, Nat. Nanotechnol. **8,** 256 (2013).

[2] T. Seifert *et al.*, Efficient metallic spintronic emitters of ultrabroadband terahertz radiation, Nat. Photonics **10,** 483 (2016).

[3] T. J. Huisman, R. V. Mikhaylovskiy, J. D. Costa, F. Freimuth, E. Paz, J. Ventura, P. P. Freitas, S. Blügel, Y. Mokrousov, T. Rasing, and A. V. Kimel, Femtosecond control of electric currents in metallic ferromagnetic heterostructures, Nat. Nanotechnol. **11,** 455 (2016).

[4] D. Yang, J. Liang, C. Zhou, L. Sun, R. Zheng, S. Luo, Y. Wu, and J. Qi, Powerful and tunable THz emitters based on the Fe/Pt magnetic heterostructure, Adv. Opt. Mater. **4,** 1944 (2016).

[5] T. Seifert, S. Jaiswal, M. Sajadi, G. Jakob, S. Winnerl, M. Wolf, M. Kläui, and T. Kampfrath, Ultrabroadband single-cycle terahertz pulses with peak fields of 300 kV cm^{-1} from a metallic spintronic emitter, Appl. Phys. Lett. **110,** 252402 (2017).

[6] Y. Wu, M. Elyasi, X. Qiu, M. Chen, Y. Liu, L. Ke, and H. Yang, High-Performance THz emitters based on ferromagnetic/nonmagnetic heterostructures, Adv. Mater. **29,** 1603031 (2017).

[7] G. Torosyan, S. Keller, L. Scheuer, R. Beigang, and E. T. Papaioannou, Optimized spintronic terahertz emitters based on epitaxial grown Fe/Pt layer structures, Sci. Rep. **8,** 1311 (2018).

[8] M. Chen, R. Mishra, Y. Wu, K. Lee, and H. Yang, Terahertz emission from compensated magnetic heterostructures, Adv. Opt. Mater. **6,** 1800430 (2018).

[9] H. S. Qiu, K. Kato, K. Hirota, N. Sarukura, M. Yoshimura, and M. Nakajima, Layer thickness dependence of the terahertz emission based on spin current in ferromagnetic heterostructures, Opt. Express **26,** 15247 (2018).

[10] R. Schneider, M. Fix, R. Heming, S. Michaelis de Vasconcellos, M. Albrecht, and R. Bratschitsch, Magnetic-Field-Dependent THz emission of spintronic TbFe/Pt layers, ACS Photonics **5,** 3936 (2018).

[11] R. Schneider, M. Fix, J. Bensmann, S. M. d. Vasconcellos, M. Albrecht, and R. Bratschitsch, Spintronic GdFe/Pt THz emitters, Appl. Phys. Lett. **115,** 152401 (2019).

[12] S. Zhang, Z. Jin, Z. Zhu, W. Zhu, Z. Zhang, G. Ma, and J. Yao, Bursts of efficient terahertz radiation with saturation effect from metal-based ferromagnetic heterostructures, J. Phys. D: Appl. Phys. **51,** 034001 (2017).

[13] J. C. R. Sánchez, L. Vila, G. Desfonds, S. Gambarelli, J. P. Attané, J. M. De Teresa, C. Magén, and A. Fert, Spin-to-charge conversion using Rashba coupling at the interface between non-magnetic materials, Nat. Commun. **4,** 2944 (2013).

[14] M. B. Jungfleisch, Q. Zhang, W. Zhang, J. E. Pearson, R. D. Schaller, H. Wen, and A. Hoffmann, Control of Terahertz Emission by Ultrafast Spin-Charge Current Conversion at Rashba Interfaces, Phys. Rev. Lett. **120,** 207207 (2018).

[15] C. Zhou, Y. P. Liu, Z. Wang, S. J. Ma, M. W. Jia, R. Q. Wu, L. Zhou, W. Zhang, M. K. Liu, Y. Z. Wu, and J. Qi, Broadband Terahertz Generation via the Interface Inverse Rashba-Edelstein Effect, Phys. Rev. Lett. **121,** 086801 (2018).

[16] M. Battiato, K. Carva, and P. M. Oppeneer, Superdiffusive Spin Transport as a Mechanism of Ultrafast Demagnetization, Phys. Rev. Lett. **105,** 027203 (2010).

[17] M. Battiato, K. Carva, and P. M. Oppeneer, Theory of laser-induced ultrafast superdiffusive spin transport in layered heterostructures, Phys. Rev. B **86,** 024404 (2012).

[18] C. R. Ast, J. Henk, A. Ernst, L. Moreschini, M. C. Falub, D. Pacilé, P. Bruno, K. Kern, and M. Grioni, Giant Spin Splitting Through Surface Alloying, Phys. Rev. Lett. **98,** 186807 (2007).

[19] Q. Zhang, Z. Luo, H. Li, Y. Yang, X. Zhang, and Y. Wu, Terahertz Emission From Anomalous Hall Effect in a Single-Layer Ferromagnet, Phys. Rev. Appl. **12,** 054027 (2019).

[20] P. C. M. Planken, H.-K. Nienhuys, H. J. Bakker, and T. Wenckebach, Measurement and calculation of the orientation dependence of terahertz pulse detection in ZnTe, J. Opt. Soc. Am. B **18,** 313 (2001).

[21] T. Tanaka, H. Kontani, M. Naito, T. Naito, D. S. Hirashima, K. Yamada, and J. Inoue, Intrinsic spin Hall effect and orbital Hall effect in 4d and 5d transition metals, Phys. Rev. B **77,** 165117 (2008).

[22] S. Krishnia, C. Murapaka, P. Sethi, W. L. Gan, Q. Y. Wong, G. J. Lim, and W. S. Lew, Current-induced spin-orbit effective field modulations in synthetic antiferromagnetic structures, J. Magn. Magn. Mater. **475,** 327 (2019).

[23] Z. Zhao, C. Papusoi, P. Mani, A. Misra, P. B. Visscher, H. Fujiwara, G. Gubbiotti, S. Tacchi, and G. J. Mankey, Effect

of variable biquadratic exchange coupling on the magnetic hysteresis of uniaxial antiferromagnetic Co/Ru/Co films, IEEE Trans. Magn. **43**, 4056 (2007).

[24] S. S. P. Parkin, N. More, and K. P. Roche, Oscillations in Exchange Coupling and Magnetoresistance in Metallic Superlattice Structures: Co/Ru, Co/Cr, and Fe/Cr, Phys. Rev. Lett. **64**, 2304 (1990).

[25] S. O. Demokritov, Biquadratic interlayer coupling in layered magnetic systems, J. Phys. D: Appl. Phys. **31**, 925 (1998).

[26] Y. Yang, Z. Luo, H. Wu, Y. Xu, R.-W. Li, S. J. Pennycook, S. Zhang, and Y. Wu, Anomalous hall magnetoresistance in a ferromagnet, Nat. Commun. **9**, 2255 (2018).

[27] Z. Luo, Q. Zhang, Y. Xu, Y. Yang, X. Zhang, and Y. Wu, Spin-Orbit Torque in a Single Ferromagnetic Layer Induced by Surface Spin Rotation, Phys. Rev. Appl. **11**, 064021 (2019).

[28] P. C. M. Planken, C. E. W. M. v. Rijmenam, and R. N. Schouten, Opto-electronic pulsed THz systems, Semicond. Sci. Technol. **20**, S121 (2005).

[29] A. Alekhin, I. Razdolski, N. Ilin, J. P. Meyburg, D. Diesing, V. Roddatis, I. Rungger, M. Stamenova, S. Sanvito, U. Bovensiepen, and A. Melnikov, Femtosecond Spin Current Pulses Generated by the Nonthermal Spin-Dependent Seebeck Effect and Interacting with Ferro-

[30] T. S. Seifert, N. M. Tran, O. Gueckstock, S. M. Rouzegar, L. Nadvornik, S. Jaiswal, G. Jakob, V. V. Temnov, M. Münzenberg, M. Wolf, M. Kläui, and T. Kampfrath, Terahertz spectroscopy for all-optical spintronic characterization of the spin-hall-effect metals Pt, W and $Cu_{80}Ir_{20}$, J. Phys. D: Appl. Phys. **51**, 364003 (2018).

[31] J. P. Wang, Z. S. Shan, S. N. Piramanayagam, and T. C. Chong, Anti-ferromagnetic coupling effects on energy barrier and reversal properties of recording media, IEEE Trans. Magn. **37**, 1445 (2001).

[32] N. Wiese, T. Dimopoulos, M. Rührig, J. Wecker, H. Brückl, and G. Reiss, Antiferromagnetically coupled CoFeB/Ru/CoFeB trilayers, Appl. Phys. Lett. **85**, 2020 (2004).

[33] J. C. A. Huang, C. Y. Hsu, S. F. Chen, C. P. Liu, Y. F. Liao, M. Z. Lin, and C. H. Lee, Enhanced antiferromagnetic saturation in amorphous CoFeB-Ru-CoFeB synthetic antiferromagnets by ion-beam assisted deposition, J. Appl. Phys. **101**, 123923 (2007).

[34] N. Wiese, T. Dimopoulos, M. Rührig, J. Wecker, and G. Reiss, Switching of submicron-sized, antiferromagnetically coupled CoFeB/Ru/CoFeB trilayers, J. Appl. Phys. **98**, 103904 (2005).